J. Fluid Mech. (2020), *vol.* 889, A13. © The Author(s), 2020.
Published by Cambridge University Press
doi:10.1017/jfm.2020.86

Streamwise-constant large-scale structures in Couette and Poiseuille flows

Simon J. Illingworth†

Mechanical Engineering, University of Melbourne, VIC 3010, Australia

(Received 23 April 2019; revised 14 January 2020; accepted 26 January 2020)

The linear amplification mechanisms leading to streamwise-constant large-scale structures in laminar and turbulent channel flows are considered. A key feature of the analysis is that the Orr–Sommerfeld and Squire operators are each considered separately. Physically, this corresponds to considering two separate processes: (i) the response of wall-normal velocity fluctuations to external forcing; and (ii) the response of streamwise velocity fluctuations to wall-normal velocity fluctuations. The analysis is performed for both plane Couette flow and plane Poiseuille flow; and for each we consider linear amplification mechanisms about both the laminar and turbulent mean velocity profiles. The analysis reveals two things. First, that the most amplified structures (with a spanwise spacing of approximately $4h$, where h is the channel half-height) are to an important degree encoded in the Orr–Sommerfeld operator alone, thus helping to explain their prevalence. Second – and consistent with numerical and experimental observations – that Couette flow is significantly more efficient than Poiseuille flow in leveraging the mean shear to produce channel-wide streamwise streaks.

Key words: turbulence modelling, shear layer turbulence

1. Introduction

Streamwise-elongated large-scale structures are prevalent in all of the canonical wall-bounded shear flows: boundary layers (Adrian, Meinhart & Tomkins 2000; Balakumar & Adrian 2007; Hutchins & Marusic 2007); pipes (Kim & Adrian 1999; Guala, Hommema & Adrian 2006; Monty *et al.* 2007, 2009); Poiseuille flow (Balakumar & Adrian 2007; Monty *et al.* 2007, 2009); and Couette flow. In this context, Couette flow is peculiar in that streamwise-elongated channel-wide structures are especially pronounced, evidence of which has been observed across a broad range of Reynolds numbers both in simulations (Lee & Kim 1991; Bech & Andersson 1994; Komminaho, Lundbladh & Johansson 1996; Papavassiliou & Hanratty 1997; Tsukahara, Kawamura & Shingai 2006; Avsarkisov *et al.* 2014; Pirozzoli, Bernardini & Orlandi 2014; Lee & Moser 2018) and in experiments (Tillmark & Alfredsson 1994; Bech & Andersson 1994; Tillmark & Alfredsson 1998; Kitoh, Nakabyashi & Nishimura 2005; Kitoh & Umeki 2008).

† Email address for correspondence: sillingworth@unimelb.edu.au

Meanwhile linear analyses of the Navier–Stokes equations also uncover an important place for streamwise-elongated structures in shear flows (Schmid & Henningson 2001). Such linear analyses reveal that, for channel flows (in which we include both Poiseuille flow and Couette flow), the structures that are most excitable are streamwise constant with a spanwise spacing of approximately $4h$, corresponding to a spanwise wavenumber of approximately $\pi/2h$ (where h is the channel half-height). This has been observed not only for laminar Couette flow and laminar Poiseuille flow (Gustavsson 1991; Butler & Farrell 1992; Farrell & Ioannou 1993; Trefethen *et al.* 1993; Jovanovic & Bamieh 2005), but also more recently for their turbulent counterparts for which the linear analyses are performed about the turbulent mean velocity profile (del Álamo & Jiménez 2006; Pujals *et al.* 2009; Hwang & Cossu 2010*a*,*b*). A key ingredient in the development of these streamwise-constant structures is the lift-up effect, the driving mechanism for which is the mean wall-normal shear (Ellingsen & Palm 1975; Landahl 1980; Kim & Lim 2000). We can therefore summarize as follows: mean shear is a key ingredient in linear amplification mechanisms; and yet the most amplified structures in channel flows are largely insensitive to the details of the shear.

This paper considers the linear amplification mechanisms leading to streamwise-constant large-scale structures in laminar and turbulent channel flows. The importance of streamwise-constant structures in channel flows has motivated a number of previous investigations using both linear (Bamieh & Dahleh 2001; Jovanovic & Bamieh 2005) and nonlinear (Gayme *et al.* 2010, 2011) modelling approaches. A key feature of the present analysis is that the Orr–Sommerfeld and Squire operators are each considered separately. (We will use a slightly modified Squire operator by setting the streamwise velocity – rather than the wall-normal vorticity – to be the output of interest.) Physically, this corresponds to considering two separate processes: (i) the response of wall-normal velocity fluctuations to external forcing; and (ii) the response of streamwise velocity fluctuations to wall-normal velocity fluctuations. Importantly, doing so allows us to define an efficiency of the overall process.

This point of view, in which the forcing of streamwise velocity by wall-normal velocity is made explicit, is in the spirit of Gustavsson (1991). It also shares some similarities with the work of Zaki & Durbin (2005) and Zaki & Durbin (2006) on bypass transition in boundary layers. The analysis is performed for both plane Couette flow and plane Poiseuille flow; and for each we consider linear amplification mechanisms about both the laminar and turbulent mean velocity profiles. By doing so we will uncover two things. First, that the most amplified structures – with a spanwise spacing of approximately $4h$ irrespective of the details of the mean flow – are to an important degree encoded in the Orr–Sommerfeld operator alone, thus helping to explain the prevalence of such structures. Second – and consistent with numerical and experimental observations – that Couette flow is significantly more efficient than Poiseuille flow in leveraging the mean shear to produce large-scale streamwise streaks.

2. Linear model

We consider laminar or turbulent flow in a channel for which the streamwise, spanwise and wall-normal directions are denoted by x, y and z; and the corresponding velocity components by u, v and w. The Reynolds number $R = u_o h/\nu$ is based on the channel half-height h, kinematic viscosity ν and some characteristic velocity u_o. For laminar flow this characteristic velocity is the maximum velocity across the channel

height; for the turbulent flow it is the friction velocity, $u_\tau = \sqrt{\tau_w/\rho}$, where τ_w is the wall shear stress and ρ is the density. Following non-dimensionalization the channel half-height is unity so that $z \in [-1, +1]$.

2.1. *Laminar velocity profiles*

The non-dimensional velocity profile for laminar Couette flow is $U(z) = z$; for laminar Poiseuille flow it is $U(z) = 1 - z^2$. Linearizing the incompressible Navier–Stokes equations about one of these laminar base flows gives

$$\frac{\partial \boldsymbol{u}}{\partial t} + U\frac{\partial \boldsymbol{u}}{\partial x} + (wU', 0, 0) = -\boldsymbol{\nabla} p + R^{-1}\Delta \boldsymbol{u} + \boldsymbol{f}, \tag{2.1a}$$

$$\boldsymbol{\nabla} \cdot \boldsymbol{u} = 0, \tag{2.1b}$$

where $\boldsymbol{u} = [u\ v\ w]^{\mathrm{T}}$ and $'$ represents differentiation in the wall-normal direction. Note the inclusion of a forcing term, $\boldsymbol{f} = [f_x\, f_y\, f_z]^{\mathrm{T}}$, in the momentum equation (2.1*a*), which we treat as an external input to the flow.

2.2. *Turbulent velocity profiles*

Linear models have been used for fully developed turbulent flows in a number of previous studies. In some the linear operator is obtained from a Reynolds decomposition of the velocity field, giving rise to a linear operator in which the viscosity is equal to the kinematic viscosity (McKeon & Sharma 2010; Sharma & McKeon 2013). In others the linear operator is obtained by first performing a triple decomposition of the velocity field and then providing a closure for the terms quadratic in the incoherent fluctuations using a simple eddy-viscosity model (Reynolds & Hussain 1972; del Álamo & Jiménez 2006; Pujals *et al.* 2009; Hwang & Cossu 2010*a*,*b*; Illingworth, Monty & Marusic 2018; Madhusudanan, Illingworth & Marusic 2019; Vadarevu *et al.* 2019). In this second case the effective viscosity, which varies across the flow, is given by the sum of the eddy and kinematic viscosities.

In this work we include only the kinematic viscosity in the linear model. Doing so gives rise to an Orr–Sommerfeld operator whose dynamics is independent of the mean velocity profile (to be made clear in § 2.3) and thus simpler and more generic than its eddy-viscosity equivalent. This choice is therefore convenient but it is also suitable for two reasons. First, a key emergent feature of both linear models is the critical layer mechanism in which a significant response can occur when the phase velocity, $c = \omega/k_x$, is equal to the local mean velocity, $c = U(z)$ (Maslowe 1986). The two linear models show different critical layer behaviours owing to their different effective viscosity profiles. But since the focus of this work is on streamwise-constant fluctuations for which the streamwise wavenumber is zero, the critical layer mechanism does not occur and this difference between the two models does not exist. Second, we must specify the variation of the eddy viscosity in the wall-normal direction (z), but a reasonable approximation is to assume instead that it is constant with z. As noted by Townsend (1956, § 6.7 p. 127), a reasonable way to determine this constant would be to compare the measured mean velocity profile with that given by assuming a suitable constant eddy viscosity; and the approximation would only be in error near the walls. It is therefore reasonable to approximate any eddy viscosity with an equivalent constant (and larger) viscosity which would manifest itself as a reduction in the effective Reynolds number R. (The effect of including an eddy viscosity in the linear model (2.1) will be considered in § 6.)

For Couette flow there is an additional reason for which the kinematic viscosity may be more appropriate than an eddy viscosity. The eddy-viscosity profile is closely related to the mean velocity profile – knowledge of one implies knowledge of the other. The strong streamwise rollers that are unique to Couette flow will surely have an influence on the mean velocity profile, and in turn on the eddy-viscosity profile. And yet the intended role of the eddy viscosity is to model the effect of small-scale, incoherent motions on the large, most energetic scales. Therefore any eddy-viscosity profile, as well as acting to modify the dynamics of the largest scales, is at the same time modified by them. This observation applies equally to Poiseuille flow and indeed any shear flow, but we can expect it to be especially problematic for Couette flow, where large-scale structures play such a prominent role.

The linear model formed about the turbulent mean flow has the same form as that for laminar flow (2.1) but the reasoning used to form it and the definition and interpretation of some its terms are different. The linear model is obtained by performing a Reynolds decomposition of the velocity field; substituting this into the incompressible Navier–Stokes equations; and subtracting the equations governing the mean flow. This gives rise to (2.1) as before but with two important differences. First, $\boldsymbol{U}$ now represents the turbulent mean velocity profile and $\boldsymbol{u}$ represents turbulent fluctuations about the mean. Second, any nonlinear terms are absorbed into the forcing term $\boldsymbol{f}$ so that $\boldsymbol{f} = -(\boldsymbol{u}\cdot\boldsymbol{\nabla})\boldsymbol{u} + \overline{(\boldsymbol{u}\cdot\boldsymbol{\nabla})\boldsymbol{u}}$ (Landahl 1967; Bark 1975; McKeon & Sharma 2010). Thus the formation of the linear operator (2.1) about the turbulent mean flow does not imply that nonlinear terms are neglected. Rather, we take the point of view that the linear operator (2.1) is constantly forced by the remaining nonlinear terms. Nonlinear effects thus manifest themselves in two ways: through their role in setting the mean velocity profile $\boldsymbol{U}$; and through their forcing of the linear operator (2.1). (The forcing could have additional contributions from any externally applied forcing as in § 2.1, but this would not modify the analysis.)

2.3. *Streamwise-constant model*

The streamwise-constant model used throughout this work is obtained by taking Fourier transforms of (2.1) in the homogeneous directions (x, y); transforming into Orr–Sommerfeld Squire form; and setting the streamwise wavenumber to zero

$$\frac{\partial \Delta \hat{w}}{\partial t} = R^{-1}\Delta^2\hat{w} - \mathrm{i}k\mathcal{D}\hat{f}_y - k^2\hat{f}_z, \tag{2.2a}$$

$$\frac{\partial \hat{u}}{\partial t} = R^{-1}\Delta\hat{u} - U'\hat{w} + \hat{f}_x, \tag{2.2b}$$

with boundary conditions $\hat{w}(t) = \partial_z\hat{w}(t) = \hat{u}(t) = 0$ at the two walls. Here k is the spanwise wavenumber, $\mathcal{D}$ represents differentiation in the wall-normal direction and $\Delta = \mathcal{D}^2 - k^2$ is the two-dimensional Laplacian. Note that, for streamwise-constant fluctuations, the equation governing the streamwise velocity $\hat{u}$ simplifies significantly. Since this is also the quantity of interest, we use it directly as the output of the Squire operator in (2.2*b*) instead of using the (standard) wall-normal vorticity. (For streamwise-constant fluctuations the relationship in Fourier space between the streamwise velocity $\hat{u}$ and the wall-normal vorticity $\hat{\eta}$ is simply $\hat{\eta} = \mathrm{i}k\hat{u}$.) Note also that we choose an evolution equation for wall-normal velocity fluctuations $\hat{w}$ in (2.2*a*) instead of $\hat{v}$ (or a suitable streamfunction) because $\hat{w}$ forces $\hat{u}$ directly in (2.2*b*).

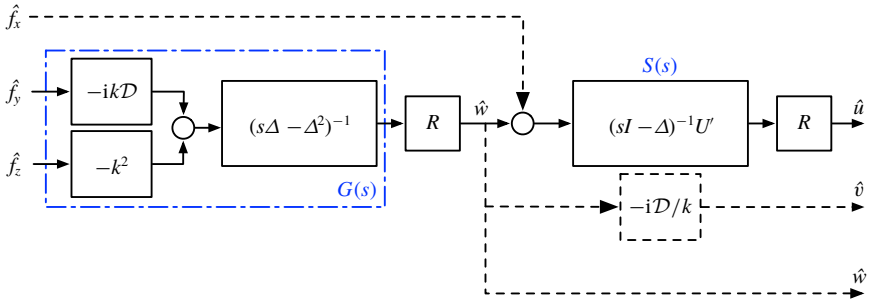

FIGURE 1. Linear amplification mechanisms for streamwise-constant fluctuations at spanwise wavenumber k. Dashed lines denote forcing components and velocity components that are omitted in the analysis. (These processes scale with R, while those retained scale with R^2 – see § 2.3.) The transfer functions $G(s)$ from (2.4*a*) and $S(s)$ from (2.4*c*) are also indicated.

$\hat{v}$ can be obtained from $\hat{w}$ by using the continuity equation (2.1*b*) with streamwise gradients set to zero (see also figure 1)

$$\mathrm{i}k\hat{v} + \mathcal{D}\hat{w} = 0. \tag{2.3}$$

Taking Laplace transforms of (2.2), rescaling the Laplace variable s by the Reynolds number R (Gustavsson 1991; Jovanovic & Bamieh 2005) and rearranging gives rise to two transfer functions, $G(s)$ and $S_o(s)$, as follows:

$$\hat{w}(s) = R \underbrace{(s\Delta - \Delta^2)^{-1}\begin{bmatrix}-\mathrm{i}k\mathcal{D} & -k^2\end{bmatrix}}_{G(s)}\begin{bmatrix}\hat{f}_y(s)\\ \hat{f}_z(s)\end{bmatrix}, \tag{2.4a}$$

$$\hat{u}(s) = R \underbrace{(sI - \Delta)^{-1}\begin{bmatrix}I & -U'\end{bmatrix}}_{S_o(s)}\begin{bmatrix}\hat{f}_x(s)\\ \hat{w}(s)\end{bmatrix}. \tag{2.4b}$$

(Rescaling the Laplace variable in this way is equivalent to rescaling time by R^{-1}.) Notice that the Reynolds number R has been isolated to render each transfer function independent of it. The transfer function $G(s)$ comes from the Orr–Sommerfeld operator. It represents the dynamics from spanwise and wall-normal forcing, $[\hat{f}_y\ \hat{f}_z]^{\mathrm{T}}$, to wall-normal velocity fluctuations, $\hat{w}$. Importantly, $G(s)$ is independent of the mean velocity profile. The transfer function $S_o(s)$ is related to the Squire operator. It represents the dynamics from streamwise forcing and wall-normal velocity fluctuations, $[\hat{f}_x\ \hat{w}]^{\mathrm{T}}$, to streamwise velocity fluctuations, $\hat{u}$. Equations (2.4) are represented in a block diagram in figure 1.

From (2.4*a*), (2.4*b*) and figure 1 we see that the overall transfer function from $[\hat{f}_y\ \hat{f}_z]^{\mathrm{T}}$ to $\hat{u}$ (which involves both $G(s)$ and $S_o(s)$) scales with R^2, while the transfer function from $\hat{f}_x$ to $\hat{u}$ (which involves only $S_o(s)$) scales with R. For sufficiently large R we can therefore neglect the influence of $\hat{f}_x$ and it is convenient to define a second transfer function, $S(s)$, for which the influence of $\hat{f}_x$ is neglected

$$\hat{u}(s) = R \underbrace{[-(sI - \Delta)^{-1}U']}_{S(s)}\hat{w}(s). \tag{2.4c}$$

The transfer function $S_o(s)$ in (2.4*b*) therefore includes the influence of $\hat{f}_x$, while the transfer function $S(s)$ in (2.4*c*) neglects it.

Finally, we define an overall transfer function $F(s)$

$$\begin{aligned} F(s) &= S(s)G(s) \\ &= (sI - \Delta)^{-1}U'(s\Delta - \Delta^2)^{-1}\begin{bmatrix} \mathrm{i}k\mathcal{D} & k^2 \end{bmatrix}. \end{aligned} \tag{2.5}$$

Implicit in (2.5) is that the contribution from streamwise forcing $\hat{f}_x$ can be ignored. This assumption is sound provided that the Reynolds number R is sufficiently large, as discussed above. Then $F(s)$ represents the overall dynamics from $[\hat{f}_y\ \hat{f}_z]^{\mathrm{T}}$ to $\hat{u}$ as follows:

$$\hat{u}(s) = R^2 F(s) \begin{bmatrix} \hat{f}_y(s) \\ \hat{f}_z(s) \end{bmatrix}. \tag{2.6}$$

The overall dynamics (2.6), together with definitions of $G(s)$ and $S(s)$, are shown in a block diagram in figure 1. Note that the Reynolds number scaling of the overall operator has also been analysed in the slightly different context of stochastic forcing for which the relevant norm (the two norm) is found to scale with $R^{3/2}$ (Bamieh & Dahleh 2001; Jovanovic & Bamieh 2005).

2.4. *Transfer function norms*

With the relevant transfer functions defined, we now introduce two norms to evaluate their size: the infinity norm $\|\cdot\|_\infty$ and the two norm $\|\cdot\|_2$.

We will make extensive use of the infinity norm, defined for a transfer function T as

$$\|T\|_\infty = \max_\omega\ \sigma_1(\mathrm{i}\omega), \tag{2.7}$$

where $\sigma_i(\mathrm{i}\omega)$ are the singular values of $T(\mathrm{i}\omega)$ at frequency ω and represent a generalization of gain for systems with many inputs and many outputs. The singular values are ordered such that $\sigma_1 \geqslant \sigma_2 \geqslant \cdots \geqslant \sigma_n$. Therefore σ_1 represents the maximum singular value at frequency ω; and the infinity norm (2.7) represents the worst-case gain over all possible forcing frequencies and forcing directions. An important property of the infinity norm – and a key reason for using it in this work – is its submultiplicative property

$$\|T_1 T_2\|_\infty \leqslant \|T_1\|_\infty \|T_2\|_\infty \tag{2.8}$$

for any two transfer functions T_1 and T_2. This property will be useful in the following sections to characterize the efficiency of the forcing of streamwise velocity fluctuations (the Squire operator S) by wall-normal velocity fluctuations (the Orr–Sommerfeld operator G).

Another commonly used norm for transfer functions is the two norm

$$\|T\|_2^2 = \frac{1}{2\pi}\int_{-\infty}^{\infty} \mathrm{Trace}[T^*(\mathrm{i}\omega)T(\mathrm{i}\omega)]\,\mathrm{d}\omega = \frac{1}{2\pi}\int_{-\infty}^{\infty}\sum_i \sigma_i^2(\mathrm{i}\omega)\,\mathrm{d}\omega. \tag{2.9}$$

The two norm (2.9) represents an average gain over all frequencies and forcing directions. In contrast to the infinity norm, the two norm does not satisfy the submultiplicative property (2.8), and is therefore less suitable for our purposes (to be made clear in § 3.2). Nevertheless, it will be used briefly in § 3 to check the sensitivity of some key results to the choice of norm.

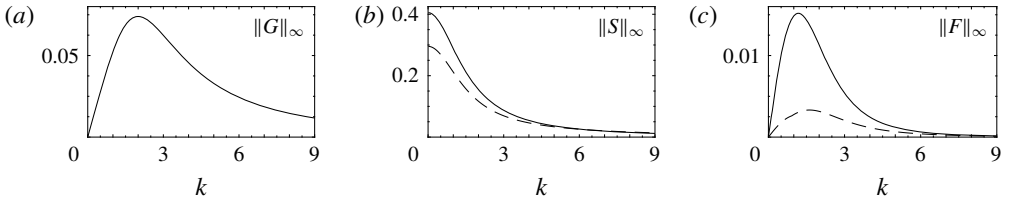

FIGURE 2. The infinity norm $\|\cdot\|_\infty$ for G (a); S (b); and $F = SG$ (c). Results for S and F are shown for Couette flow (——) and for Poiseuille flow (– –).

2.5. *Numerical discretization*

Equations (2.4*a*) and (2.4*c*) are discretized in the wall-normal direction (z) using Chebyshev collocation. A total of 101 Chebyshev points are used, which is sufficient for the large scales of interest. Convergence has been checked by doubling the number of Chebyshev points and ensuring that the results do not change. The norms (2.7) and (2.9) are defined such that they each correspond to grid-independent energy norms. This is achieved using Clenshaw–Curtis quadrature (Trefethen 2008).

3. Laminar velocity profiles

We start by evaluating the infinity norm (2.7) for laminar Couette flow and laminar Poiseuille flow as a function of the spanwise wavenumber k. We do this for the Orr–Sommerfeld operator G (2.4*a*), the Squire operator S (2.4*c*) and for the overall operator $F = SG$ (2.5).

3.1. *Norms of G, S and F with spanwise wavenumber*

Figure 2 plots the infinity norm (2.7) as a function of spanwise wavenumber for G, S and F. We plot all norms only for non-zero values of k since, when $k = 0$, the continuity equation becomes simply $\partial w/\partial z = 0$, which, together with the boundary conditions for w, implies that $w = 0$ everywhere. Recall from § 2.3 that the Reynolds number R has been isolated from each transfer function (see (2.4) and (2.6)). This means that all results effectively correspond to $R = 1$. This, coupled with the fact that the infinity norm satisfies $\|RT(s)\|_\infty = R\|T(s)\|_\infty$ for any transfer function $T(s)$ (and R positive), means that the results at any Reynolds number can be readily generated from the results presented here. The infinity norm of the Orr–Sommerfeld operator G is plotted in figure 2(*a*). Recall that, for streamwise-constant fluctuations, the dynamics of G is independent of the mean velocity profile and is therefore identical for Poiseuille flow and Couette flow. We observe that $\|G\|_\infty$ attains its maximum at a spanwise wavenumber of $k = 2.00$ ($\lambda = 3.14$). The infinity norm of the Squire operator S is plotted in figure 2(*b*). Notice that there are now two curves – one for Couette flow and one for Poiseuille flow – because S is a function of the mean velocity profile. For both flows $\|S\|_\infty$ attains its maximum at $k = 0$ and decreases monotonically with increasing k. Finally, the infinity norm of $F = SG$, which represents the overall dynamics, is plotted in figure 2(*c*). For both flows $\|F\|_\infty$ attains its maximum near $k \approx \pi/2$ ($\lambda \approx 4$). Precisely, $\|F\|_\infty$ attains its maximum at $k = 1.18$ ($\lambda = 5.3$) for Couette flow and at $k = 1.62$ ($\lambda = 3.9$) for Poiseuille flow.

What if we use a different norm? Table 1 summarizes the spanwise wavenumbers at which the peak response, as measured by the infinity norm, is achieved; and also

	G	S_{coue}	S_{pois}	F_{coue}	F_{pois}
k_{max} for $\|\cdot\|_\infty$	2.00	0	0	1.18	1.62
k_{max} for $\|\cdot\|_2$	2.90	0	0	1.40	1.79

TABLE 1. Spanwise wavenumber k_{max} at which the largest response occurs for the infinity norm, $\|\cdot\|_\infty$, and the two norm, $\|\cdot\|_2$.

repeats this using the two norm (2.9). (The variation of the two norm with k is plotted in the Appendix.) When rescaled by R, the infinity norm of the overall operator F is equivalent to the 'maximum resonance' for $R \to \infty$ as plotted in table 1 of Trefethen *et al.* (1993). (The limiting case of $R \to \infty$ is equivalent to neglecting the influence of $\hat{f}_x$, as done in § 2.3.) Similarly, when properly rescaled by R, the two norm of the overall operator F is equivalent to the variance of the response to stochastic forcing of unit power, as considered in Farrell & Ioannou (1993) and Jovanovic & Bamieh (2005) (although in those studies the influence of $\hat{f}_x$ was not neglected). From table 1 and the Appendix we see that the responses of the operators G, S and F, as measured by the two norm, show similar behaviour to that seen using the infinity norm. In particular, we still observe (i) that G and F each attain their maximum response at a spanwise wavenumber $k \approx 2$; and (ii) that S attains its maximum response at $k = 0$. Thus we see that pertinent results observed when using the infinity norm are also observed when using the two norm, and therefore that these features are not an artefact of our particular choice of norm.

From figure 2 it is interesting that, despite the norm $\|G\|_\infty$ remaining unchanged and the norm $\|S\|_\infty$ remaining similar across the two flows, the norm of the overall system, $\|F\|_\infty$ differs significantly. In particular $\|F\|_\infty$ for Couette flow is significantly larger than $\|F\|_\infty$ for Poiseuille flow. We now consider this in more detail by defining an efficiency of the forcing process.

3.2. *Efficiency*

We now make use of the submultiplicative property of the infinity norm (see § 2.4)

$$\|F\|_\infty = \|SG\|_\infty \leqslant \|S\|_\infty \|G\|_\infty. \tag{3.1}$$

In words: the optimal response of the overall system, when quantified using the infinity norm, is at most as large as the product of the optimal responses of the two systems of which it is composed. How closely equality in (3.1) is approached is determined by the nature of the interaction between G and S. With (3.1) in mind we now introduce an efficiency, α, defined such that

$$\|SG\|_\infty = \alpha \|S\|_\infty \|G\|_\infty, \tag{3.2}$$

or

$$\alpha = \frac{\|SG\|_\infty}{\|S\|_\infty \|G\|_\infty}. \tag{3.3}$$

Note that (3.1) and (3.2) together imply that $\alpha \leqslant 1$. A value of $\alpha = 1$ implies that the forcing of streamwise velocity fluctuations by wall-normal velocity fluctuations is perfectly efficient. A value of $\alpha \approx 0$ implies a low efficiency or that wall-normal

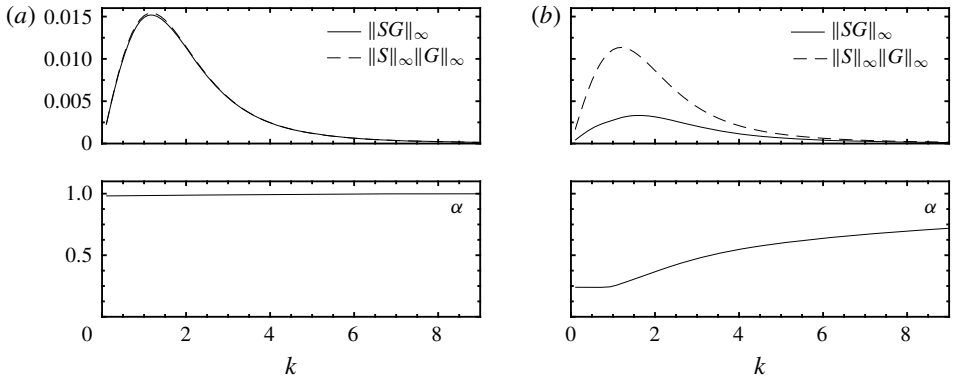

FIGURE 3. The infinity norm of the overall system, $\|F\|_\infty = \|SG\|_\infty$, and its upper bound $\|S\|_\infty\|G\|_\infty$; and the corresponding forcing efficiency α (3.3). Results are shown for Couette flow (*a*) and for Poiseuille flow (*b*).

velocity fluctuations (G) are not able in turn to easily excite streamwise velocity fluctuations (S).

It is important now to clarify (i) the physical significance of the efficiency α; (ii) the specific sense in which it represents an efficiency; and (iii) the ways in which it might give additional insight over more standard analyses such as transient growth. It is instructive to think of the mean flow – and in particular the mean shear – as the fuel for velocity fluctuations. We might expect that the energy extracted from a fuel will be much greater than the initial energy required to extract it. (A simple everyday example would be the energy expended in pressing an accelerator pedal versus the energy extracted to accelerate an entire car.) If we were to define the efficiency of such a process as the ratio of the energy extracted to the energy expended, then we would expect this efficiency to be much greater than one. This is not the sense in which α in (3.3) represents an efficiency. Rather, α represents a measure of the energy extracted from the fuel when compared to the energy available in that fuel. This can give additional insight since, in more standard analyses, we gain information on the energy of fluctuations when compared to the energy input, but not on the energy of fluctuations when compared to the energy that is available. It is for this reason that α can serve as a useful additional metric.

Figure 3 shows the numerator and denominator of (3.3), together with the efficiency α, for both Couette flow and Poiseuille flow. From (3.1) we expect that the denominator, $\|S\|_\infty\|G\|_\infty$, will serve as an upper bound for the numerator, $\|SG\|_\infty$ and this is confirmed in panels (*a*,*b*). For Couette flow the upper bound is very nearly attained (panel (*a*)) corresponding to an efficiency α close to 1 (panel (*b*)). For Poiseuille flow the efficiency is considerably less than 1 at all spanwise wavenumbers considered and is in the region of $\alpha \approx 0.4$ for the spanwise wavenumbers at which the largest overall response is attained (i.e. $k \approx \pi/2$).

4. Turbulent velocity profiles

We now repeat the analysis of § 3 using turbulent mean velocity profiles for both Couette flow and Poiseuille flow. The focus of the results is similar to that of § 3, with the caveat that the mean velocity profile – and therefore the models S and F – now vary with Reynolds number. (Recall from § 2.3 that the Reynolds number has

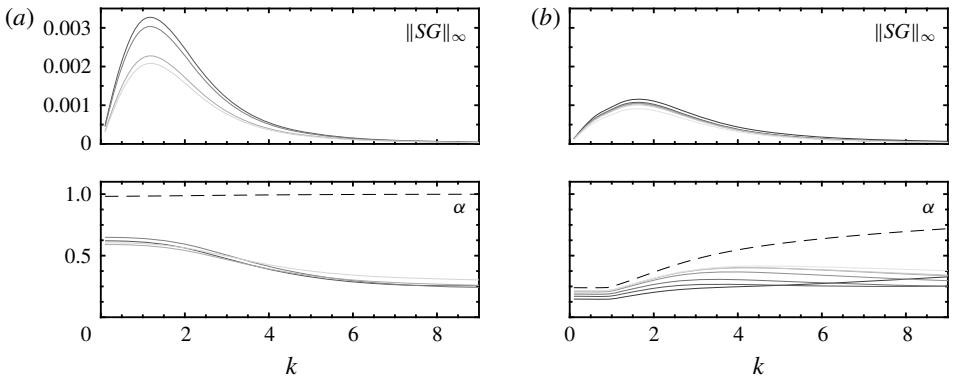

FIGURE 4. The infinity norm of the overall system, $\|F\|_\infty = \|SG\|_\infty$, as a function of the spanwise wavenumber k; and the efficiency, α as defined in (3.3). Results are shown for Couette flow (*a*) and for Poiseuille flow (*b*). Lighter lines correspond to larger friction Reynolds numbers R_τ. For comparison the efficiencies α for laminar flow from figure 3 are also plotted (– –).

Couette	R_τ	—	171	260	507	—	986
Poiseuille	R_τ	107	180	298	550	816	950

TABLE 2. Friction Reynolds numbers considered.

been eliminated from the operators G, S and F; therefore the turbulent Reynolds number manifests itself only through the modification of the mean velocity profile.) The turbulent mean velocity profiles are taken from existing turbulence databases (Hoyas & Jiménez 2006, 2008; Pirozzoli *et al.* 2014, 2017). The Reynolds numbers considered are summarized in table 2. For Couette flow we use data for friction Reynolds numbers R_τ between 171 and 986. For Poiseuille flow we use data for friction Reynolds numbers between 107 and 950.

In figure 4 we plot (for each Reynolds number) the infinity norm of the overall system, $\|F\|_\infty = \|SG\|_\infty$, as a function of the spanwise wavenumber k. We also plot for each Reynolds number the efficiency, α, as defined in (3.3). For comparison we include the plots of α for laminar flow from figure 3 (dashed lines). ($\|S\|_\infty\|G\|_\infty$ is not plotted but can be inferred from knowledge of $\|SG\|_\infty$ and α.) We see that, for both flows and for all Reynolds numbers, a peak in $\|SG\|_\infty$ occurs for spanwise wavenumbers in the vicinity of $k = \pi/2$, as it did for laminar flow in figure 3, and consistent with previous work (Pujals *et al.* 2009; Hwang & Cossu 2010*a*,*b*). This is perhaps not surprising: recall from figure 2 that this peak is present in $G(s)$ governing the wall-normal velocity, which from (2.4*a*) is independent of the mean velocity profile and therefore has identical dynamics across all laminar and turbulent flows. These results are in good agreement with direct numerical simulations (DNS) and experiments, where the spanwise dimensions of the channel-wide streamwise streaks are in the approximate range of $\lambda \approx 4$–$5h$ ($k = 1.26$–1.57) (Pirozzoli *et al.* 2014). We also see in figure 4 that the efficiencies, α, are lower than their laminar counterparts for all of the turbulent Reynolds numbers considered.

Key results from figure 4 are summarized as a function of Reynolds number in figure 5. We plot in panel (*a*) the spanwise wavenumber k_{max} at which $\|SG\|_\infty$ attains

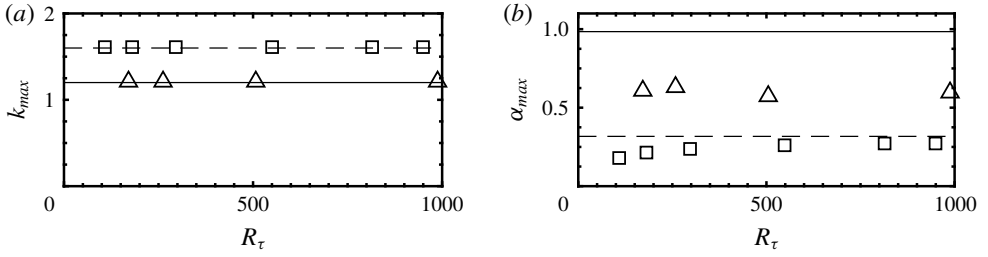

FIGURE 5. Summary of key results from figure 4 as a function of friction Reynolds number R_τ: (*a*) spanwise wavenumber, k_{max}, at which $\|F\|_\infty$ attains its maximum; and (*b*) the efficiency, α_{max}, attained at this maximum. Results are shown for turbulent Couette flow (△), turbulent Poiseuille flow (□) and their laminar counterparts (Couette ——, Poiseuille – –).

its maximum; and in panel (*b*) the efficiency α_{max} attained at this maximum. We also plot these same quantities for the laminar velocity profiles (dashed lines) for comparison. For both flows we see that k_{max} remains almost constant as the friction Reynolds number is varied. For Couette flow it lies in the range $1.18 \leqslant k_{max} \leqslant 1.19$; for Poiseuille flow it occurs at $k_{max} = 1.62$ for all cases considered (including the laminar flow). For both flows the efficiency α_{max} at this spanwise wavenumber is lower for the turbulent velocity profiles than it is for their laminar counterparts. For Couette flow it reduces from $\alpha_{max} = 0.98$ for the laminar profile to lie in the range $0.58 \leqslant \alpha_{max} \leqslant 0.63$ for the turbulent mean profiles. For Poiseuille flow it reduces from $\alpha_{max} = 0.32$ for the laminar profile to lie in the range $0.21 \leqslant \alpha_{max} \leqslant 0.28$ for the turbulent mean profiles. Despite the greater reductions for Couette flow, α_{max} is nonetheless larger for Couette flow than it is for Poiseuille flow for all cases considered. Indeed the maximum α_{max} attained for Poiseuille flow is still smaller than the minimum value attained for Couette flow by a factor of approximately two (figure 5*b*).

5. Singular value decomposition of G and S at $\omega = 0$

We have seen that the efficiency of the forcing process, as characterized by the quantity α, is significantly higher for Couette flow than it is for Poiseuille flow for both laminar and turbulent mean velocity profiles. We now seek to explain this observation by performing singular value decompositions of the discretized Orr–Sommerfeld and Squire operators, G and S.

As described in § 2.4, the infinity norm (2.7) of a transfer function represents a maximum (or worst-case) gain. This is attained at a particular forcing frequency and for a particular forcing direction, and therefore any analysis of $\|G\|_\infty$, $\|S\|_\infty$ and $\|F\|_\infty$ is complicated by the fact that each can occur at different temporal frequencies ω. For streamwise-constant fluctuations, however, the infinity norms $\|G\|_\infty$, $\|S\|_\infty$ and $\|F\|_\infty$ all occur at zero frequency, $\omega = 0$. We therefore need only consider each transfer function at $\omega = 0$, i.e. $G(\mathrm{i}0)$, $S(\mathrm{i}0)$ and $F(\mathrm{i}0)$. A singular value decomposition of $G(\mathrm{i}0)$ is then

$$G(\mathrm{i}0) = U \Sigma V^*, \tag{5.1}$$

(and similarly for S) where $\Sigma = \mathrm{diag}[\sigma_1 \ \cdots \ \sigma_n]$ contains the singular values with $\sigma_1 \geqslant \sigma_2 \geqslant \cdots \geqslant \sigma_n$; $U = [u_1 \ \cdots \ u_n]$ contains the response singular vectors; and $V = [v_1 \ \cdots \ v_n]$ contains the forcing singular vectors. Now writing the product of the two

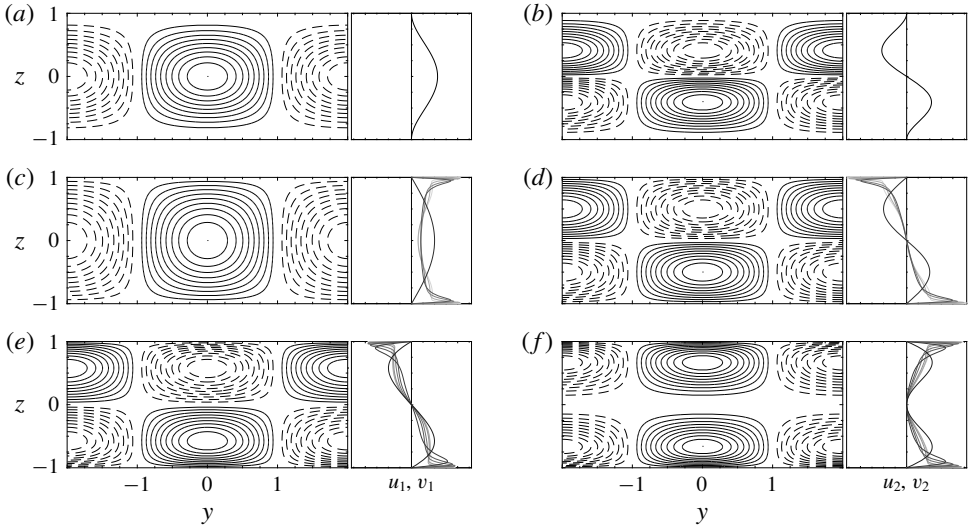

FIGURE 6. (*a*,*b*) First two singular response modes (u_1, u_2) of G; and first two singular forcing modes (v_1 and v_2) of S for Couette flow (*c*,*d*) and Poiseuille flow (*e*,*f*). In each panel the singular modes are shown in physical space on the left (laminar velocity profiles only); and in Fourier space on the right (laminar and turbulent velocity profiles; lighter lines correspond to larger friction Reynolds numbers). In each plot the scaling is arbitrary.

transfer functions G and S in terms of their singular value decompositions (using subscripts to distinguish between them)

$$F(\mathrm{i}0) = S(\mathrm{i}0)G(\mathrm{i}0) = U_S \Sigma_S V_S^* U_G \Sigma_G V_G^*, \tag{5.2}$$

from which we see that key roles will be played by U_G (the singular response modes of G) and by V_S (the singular forcing modes of S) since their product $V_S^* U_G$ appears at the centre of (5.2). The quantity $V_S^* U_G$ thus quantifies the nature of the interaction between the Orr–Sommerfeld and Squire operators, G and S.

5.1. *Leading singular modes of G and S*

Given the importance of U_G and V_S in determining the interaction between G and S, we now plot their variation in the wall-normal direction. We do so for Couette flow and Poiseuille flow and for their laminar and turbulent velocity profiles. In all cases we set the spanwise wavenumber to $k = \pi/2$, which lies approximately in the range where the infinity norm of the overall operator, $\|F\|_\infty$, achieves its largest value. We plot only the first two singular modes of both operators because, as we will see, these are the most significant for explaining the results of §§ 3 and 4.

The first two singular response modes (u_1 and u_2) of the Orr–Sommerfeld operator G are shown in figure 6(*a*,*b*). (These are plotted in physical space, $u_i(y, z)$, on the left and in Fourier space, $u_i(k = \pi/2, z)$, on the right of each panel.) Recall that, for streamwise-constant fluctuations, the Orr–Sommerfeld operator is independent of the mean velocity profile. Therefore u_1 and u_2 remain the same across all of the velocity profiles that we consider (Couette and Poiseuille; laminar and turbulent). The first response mode, u_1, spans the entire channel height and is symmetric about the

	Couette				Poiseuille			
	Laminar		$R_\tau = 986$		Laminar		$R_\tau = 950$	
	v_1^*	v_2^*	v_1^*	v_2^*	v_1^*	v_2^*	v_1^*	v_2^*
u_1	0.985	0	0.544	0	0	0.515	0	0.385
u_2	0	0.971	0	0.496	0.931	0	0.806	0

TABLE 3. Summary of the inner products $v_i^* u_j$ for $i, j = 1, 2$ (equivalent to looking at the first two diagonal entries of $V_S^* U_G$).

channel centre (reaching its peak response there). The second response mode, u_2, is anti-symmetric about the channel centre (where it is zero).

The first two singular forcing modes (v_1 and v_2) of the Squire operator S for laminar Couette flow are shown in figure 6(*c*,*d*). (Again, these are plotted both in Fourier space and in physical space.) The first forcing mode v_1 is symmetric about the channel centre and is similar to u_1; and the second forcing mode v_2 is anti-symmetric about the channel centre and is similar to u_2. This similarity between the leading forcing modes of G and the leading response modes of S can be quantified by looking at the inner products $v_1^* u_1$ and $v_2^* u_2$. (This is equivalent to looking at the first two diagonal entries of $V_S^* U_G$.) These are $v_1^* u_1 = 0.985$ and $v_2^* u_2 = 0.971$. (The maximum possible value is 1 since U_G and V_S are each orthonormal.) These values are also summarized in table 3.

The story is quite different for laminar Poiseuille flow. The first two singular forcing modes (v_1 and v_2) of the Squire operator S for laminar Poiseuille flow are shown in figure 6(*e*,*f*). The first forcing mode, v_1, is anti-symmetric about the channel centre; while the second forcing mode, v_2 is symmetric. The anti-symmetry of v_1 means that its inner product with u_1 (which is symmetric) is zero, $v_1^* u_1 = 0$. Thus the different symmetries of laminar Poiseuille flow mean that the leading forcing mode of the Squire operator is not excited by the leading response mode of the Orr–Sommerfeld operator. (The two modes are orthogonal.) In a similar way, the symmetry of v_2 means that its inner product with u_2 (which is anti-symmetric) is zero, $v_2^* u_2 = 0$. Thus for Poiseuille flow the important interactions are the second response mode with the first forcing mode ($v_1^* u_2 = 0.931$); and the first response mode with the second forcing mode ($v_2^* u_1 = 0.515$). This limits the forcing efficiency of laminar Poiseuille flow and is a consequence of its anti-symmetrical shear profile U'.

Similar arguments apply when we replace the laminar velocity profiles of § 3 with the turbulent mean velocity profiles of § 4. In particular the first forcing mode v_1 of the Squire operator is symmetric for turbulent Couette flow and anti-symmetric for turbulent Poiseuille flow; and the second forcing mode v_2 is anti-symmetric for turbulent Couette flow and symmetric for turbulent Poiseuille flow. These first two forcing modes are shown in figure 6(*c–f*) for all Reynolds numbers considered alongside their laminar counterparts. (For brevity they are shown only in Fourier space.) Thus the symmetries observed in the leading forcing modes of S for laminar Couette flow and laminar Poiseuille flow are retained by their turbulent counterparts. The most notable difference is that, for the turbulent mean velocity profiles, the leading forcing modes display peaks near the channel walls. These peaks occur for both Couette flow and Poiseuille flow and they move closer to the wall as Reynolds number increases. This is not surprising given the crucial role of the mean wall-normal shear for the Squire operator – and that this shear becomes increasingly concentrated

at the wall with increasing Reynolds number. This in turn causes a reduction in the inner products considered earlier. For Couette flow the inner product $v_1^* u_1$ reduces from 0.985 (laminar) to 0.544 ($R_\tau = 986$); and the inner product $v_2^* u_2$ reduces from 0.971 (laminar) to 0.496 ($R_\tau = 986$). For Poiseuille flow the inner product $v_2^* u_1$ reduces from 0.515 (laminar) to 0.385 ($R_\tau = 950$); and the inner product $v_1^* u_2$ reduces from 0.931 (laminar) to 0.806 ($R_\tau = 950$). (These values are also summarized in table 3.) This indicates (for both flows) a reduction in the projection of the leading response modes of G onto the leading forcing modes of S and helps to explain the reduced efficiency α for the turbulent mean velocity profiles observed in figures 4 and 5.

We finish this section by considering why laminar Couette flow displays almost perfect forcing efficiency, $\alpha \approx 1$. This is explained by the fact that, for laminar Couette flow, the shear profile satisfies $U'(z) = 1$ everywhere. Thus the Squire operator becomes simply $S = (sI - \Delta)^{-1}$, the dynamics of which is similar to that of $(s\Delta - \Delta^2)^{-1}$, which appears in the Orr–Sommerfeld operator $G(s)$ (see (2.4*a*)). It is then perhaps not surprising that the leading forcing modes of S in figure 6(*a*,*b*) are so similar to the leading response modes of G in figure 6(*c*,*d*). More generally (not shown) the ith forcing mode of S is similar to the ith response mode of G and thus the inner product $v_i^* u_i$ is close to unity.

6. Effect of including an eddy viscosity

The results presented in §§ 4 and 5 (for turbulent mean velocity profiles) use the kinematic viscosity in the linear model (2.1). This choice of the kinematic viscosity (rather than an eddy viscosity) was discussed and justified in § 2.2. In particular: (i) it leads to a simpler and more generic linear model; (ii) it is appropriate for streamwise-constant fluctuations, which are our focus; and (iii) it would be reasonable to approximate any eddy viscosity with an equivalent constant viscosity, which would appear simply as a reduction in the effective Reynolds number R in the linear model (2.1). Our choice of a constant viscosity in the linear model (2.1) is therefore well motivated. However, it is also interesting to consider the effect of including an eddy viscosity in the linear model (2.1), not least because this approach has formed the basis of a number of previous studies concerning linear mechanisms in wall turbulence as discussed in § 2.2.

The linear model (2.2), when an eddy viscosity is included, becomes

$$\frac{\partial \Delta \hat{w}}{\partial t} = \mathcal{L}_{OS}\hat{w} - \mathrm{i}k\mathcal{D}\hat{f}_y - k^2\hat{f}_z, \tag{6.1a}$$

$$\frac{\partial \hat{u}}{\partial t} = \mathcal{L}_{SQ}\hat{u} - U'\hat{w} + \hat{f}_x, \tag{6.1b}$$

where $\mathcal{L}_{OS}$ and $\mathcal{L}_{SQ}$ are the Orr–Sommerfeld and Squire operators for streamwise-constant perturbations and for an eddy-viscosity profile, ν_T, that varies in the wall-normal direction

$$\mathcal{L}_{OS} = \nu_T\Delta^2 + 2\nu_T'\mathcal{D}\Delta + \nu_T''(\mathcal{D}^2 + k^2), \tag{6.2a}$$

$$\mathcal{L}_{SQ} = \nu_T\Delta + \nu_T'\mathcal{D}. \tag{6.2b}$$

Notice that, since the viscosity now varies in the wall-normal direction, we cannot isolate it in the way we isolated the Reynolds number R for the linear model (2.1)

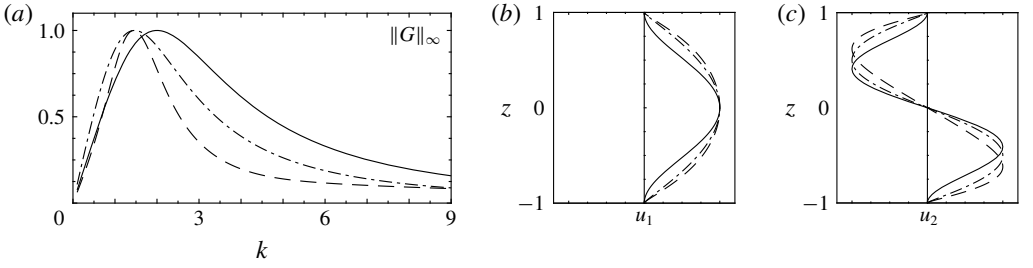

FIGURE 7. (*a*) The infinity norm of the Orr–Sommerfeld operator, $\|G\|_\infty$; and (*b,c*) wall-normal variation of the (*b*) first and (*c*) second response modes of G. In each panel results are shown for the linear model with kinematic viscosity (2.2) (solid lines) and for the linear model with eddy viscosity (6.1) for Couette flow (dashed lines) and Poiseuille flow (dot–dashed lines). In (*b,c*) the scaling is arbitrary.

with kinematic viscosity. Using the scaling arguments of § 2.3, we again ignore the influence of the streamwise forcing, $\hat{f}_x$, in (6.1*b*) so that the Squire operator S is forced only by the wall-normal velocity $\hat{w}$. (Although the effective Reynolds number will be reduced by the eddy viscosity, it should still be sufficiently high for the scaling arguments of § 2.3 to be applicable.)

6.1. *Effect on the Orr–Sommerfeld operator G*

We observed in § 2.3 that, for the kinematic viscosity, the Orr–Sommerfeld operator $G(s)$ is independent of the mean velocity profile and is therefore identical for Couette flow and Poiseuille flow. This is no longer true for the linear model (6.1) because the operator $G(s)$ now depends on the eddy-viscosity profile, which itself depends on the mean velocity profile. This ultimately means that we must now compare three linear operators: (i) G using the kinematic viscosity (valid for both flows); (ii) G for Couette flow with eddy viscosity; and (iii) G for Poiseuille flow with eddy viscosity. For simplicity we do this comparison only for the largest friction Reynolds number available – for which we expect the influence of the eddy viscosity to be most significant. For Couette flow this is $R_\tau = 986$ and for Poiseuille flow it is $R_\tau = 950$.

Figure 7 summarizes the influence of the eddy viscosity on the Orr–Sommerfeld operator $G(s)$. In panel (*a*) we plot the infinity norm, $\|G\|_\infty$ with spanwise wavenumber k for the three operators. The three curves have each been normalized by their maximum value to aid comparison. We see that including an eddy viscosity reduces the spanwise wavenumber at which the peak response occurs: for the kinematic viscosity this peak occurs at $k_{max} = 2.00$; with eddy viscosity the peak reduces to $k_{max} = 1.44$ for Couette flow and to $k_{max} = 1.47$ for Poiseuille flow. Therefore including an eddy viscosity in the linear operator does modify the behaviour of the Orr–Sommerfeld operator G. But this modification is relatively small and we ultimately draw the same conclusion as we did for the kinematic viscosity: that the Orr–Sommerfeld operator has a preferred spanwise wavenumber; and that this is in the region of $k \approx 1$–2. In panels (*b,c*) we plot the first two singular response modes of G for the three cases. We see that including an eddy viscosity in the linear operator modifies these response modes. But again, this modification is relatively small and we ultimately draw the same conclusions as we did for the kinematic viscosity: that both response modes are channel-wide; that the first response mode is symmetric

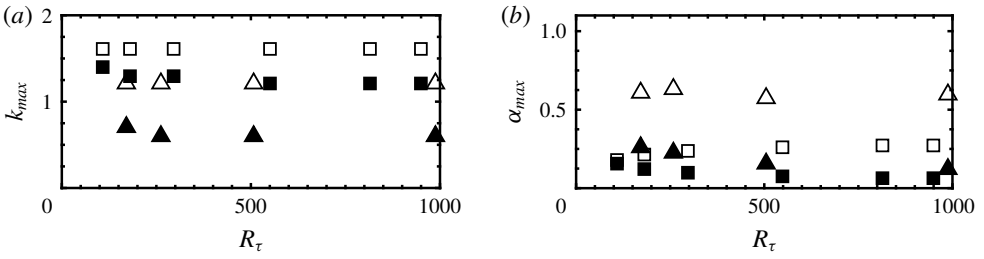

FIGURE 8. Summary of key results for the linear model with eddy viscosity (6.1) as a function of friction Reynolds number R_τ: (*a*) spanwise wavenumber, k_{max}, at which $\|F\|_\infty$ attains its maximum; and (*b*) the efficiency, α_{max}, attained at this maximum. Results are shown for turbulent Couette flow (▲) and turbulent Poiseuille flow (■). Results from figure 5 for the linear model with kinematic viscosity (2.2) are also shown (△, □).

about the channel centre; and that the second response mode is anti-symmetric about the channel centre.

6.2. *Effect on k_{max} and α_{max}*

We now consider the effect of the eddy viscosity on the overall operator $F(s)$. In particular, we will look at the influence on the spanwise wavenumber at which $\|F\|_\infty$ attains its maximum (k_{max}); and the efficiency attained at this maximum (α_{max}). In other words we repeat here the results of figure 5 using the linear model (6.1) so that an eddy viscosity is included in the overall operator $F(s)$.

The results are plotted in figure 8. We plot in panel (*a*) the spanwise wavenumber k_{max} at which $\|F\|_\infty$ attains its maximum; and in panel (*b*) the efficiency α_{max} attained at this maximum. We also plot these same quantities for the laminar velocity profiles (dashed lines) and for the turbulent velocity profiles without eddy viscosity (open symbols), which were also plotted in figure 5. In panel (*a*) we see that, for both flows, the effect of including an eddy viscosity is to reduce k_{max}. For Poiseuille flow the reduction in k_{max} is at most 25 % (from $k_{max} = 1.60$ to $k_{max} = 1.2$ at $R_\tau = 950$). For Couette flow the reduction in k_{max} is much larger: the largest reduction is 50 % (from $k_{max} = 1.2$ to $k_{max} = 0.6$ at $R_\tau = 986$). This is broadly consistent with the results obtained by Hwang & Cossu (2010*a*). Using the linearized Navier–Stokes equations for Couette flow at a lower friction Reynolds number of $R_\tau = 52$, they found a preferred spanwise wavenumber for harmonic forcing (the infinity norm) of $k_{max} = 0.82$ (which corresponds to a spanwise wavelength of $\lambda_{max} = 7.7h$). These results are all in quite poor agreement with DNS and experiments, where the spanwise dimensions of the channel-wide streamwise streaks are in the approximate range of $\lambda \approx 4$–$5h$ ($k = 1.26$–1.57) (Pirozzoli *et al.* 2014). It seems, then, that the eddy viscosity is less appropriate for Couette flow – at least for streamwise-constant modes – and this is likely in part for the reasons discussed earlier in § 2.2.

In panel (*b*) we see that, for both flows, including an eddy viscosity significantly reduces α_{max}. To give some indication, the average value of α_{max} across all turbulent Reynolds numbers reduces from 0.24 to 0.09 for Poiseuille flow; and from 0.60 to 0.19 for Couette flow. Despite this, it is important to stress that the efficiency achieved by Couette flow is still in every case larger than that for Poiseuille flow by a factor of approximately 2. Thus although the efficiency of both flows is reduced by the inclusion of an eddy viscosity, the efficiencies of the two flows relative to each

other remains approximately the same. (Specifically, at the highest Reynolds numbers available, the ratio of efficiencies is 2.15 when using the kinematic viscosity and is 2.09 when using the eddy viscosity.) We can therefore still conclude that Couette flow is significantly more efficient than Poiseuille flow, even if the efficiency of both flows is reduced.

7. Conclusions

We have considered the linear amplification mechanisms leading to streamwise-constant large-scale structures in laminar and turbulent channel flows. To do so, the Orr–Sommerfeld and Squire operators have each been considered separately. This is advantageous in three ways: (i) it makes explicit the forcing of streamwise velocity fluctuations by wall-normal velocity fluctuations; (ii) it allows one to define an efficiency of this forcing process, and therefore to characterize the energy extracted by fluctuations when compared to the energy available in the mean shear; and (iii) it exploits the fact that, for streamwise-constant fluctuations, the dynamics governing the wall-normal velocity is independent of the mean velocity profile (and therefore the mean shear). The analysis helps to explain the prevalence of streamwise-constant structures with a spanwise spacing of approximately $4h$ (where h is the channel half-height) in both laminar and turbulent channel flows. This spanwise spacing is encoded in the Orr–Sommerfeld operator $G(s)$ (figure 2) which, for streamwise-constant fluctuations, depends only on the channel geometry and boundary conditions. The analysis also indicates that Couette flow is more efficient than Poiseuille flow in leveraging the mean shear to produce channel-wide streamwise streaks. This helps to explain the energetic large-scale roll modes observed in Couette flows over a wide range of Reynolds numbers. The effect of including an eddy viscosity was also considered. Although the eddy viscosity does serve to reduce the overall forcing efficiency, we still observe that Couette flow is significantly more efficient than Poiseuille flow in leveraging the mean shear to produce channel-wide streamwise streaks. (The spanwise wavenumbers at which the maximum response is obtained for Couette flow with eddy viscosity do, however, show poorer agreement with observations.)

As well as being of interest from a modelling point of view, the analysis could also have implications for control. For example, one way to reduce the propensity for large-scale roll modes – as demonstrated by Poiseuille flow – is to use boundary conditions such that the dynamics governing the wall-normal velocity and the dynamics governing the streamwise velocity have different symmetries. While this might suggest possibilities that are ultimately impractical, at its best it could uncover possibilities that would otherwise be missed.

Acknowledgements

I am grateful for the financial support of the Australian Research Council.

Declaration of interests

The authors report no conflict of interest.

Appendix. Two norm of G, S and F with spanwise wavenumber

The two norms (2.9) of G, S and F as a function of the spanwise wavenumber k are plotted in figure 9. (The spanwise wavenumbers at which the peak in the two norm occurs are summarized in table 1 in § 3.1.)

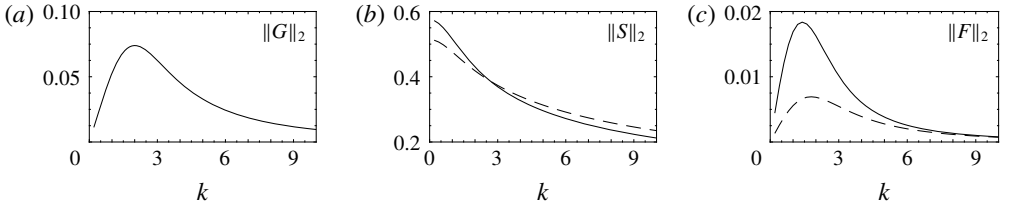

FIGURE 9. The two norm $\|\cdot\|_2$ for G (*a*); S (*b*); and $F = SG$ (*c*). Results for S and F are shown for Couette flow (——) and for Poiseuille flow (– –).

REFERENCES

ADRIAN, R. J., MEINHART, C. D. & TOMKINS, C. D. 2000 Vortex organization in the outer region of the turbulent boundary layer. *J. Fluid Mech.* **422**, 1–54.

DEL ÁLAMO, J. C. & JIMÉNEZ, J. 2006 Linear energy amplification in turbulent channels. *J. Fluid Mech.* **559**, 205–213.

AVSARKISOV, V., HOYAS, S., OBERLACK, M. & GARCÍA-GALACHE, J. P. 2014 Turbulent plane Couette flow at moderately high Reynolds number. *J. Fluid Mech.* **751**, R1.

BALAKUMAR, B. J. & ADRIAN, R. J. 2007 Large-and very-large-scale motions in channel and boundary-layer flows. *Phil. Trans. R. Soc. Lond.* A **365** (1852), 665–681.

BAMIEH, B. & DAHLEH, M. 2001 Energy amplification in channel flows with stochastic excitation. *Phys. Fluids* **13** (11), 3258–3269.

BARK, F. H. 1975 On the wave structure of the wall region of a turbulent boundary layer. *J. Fluid Mech.* **70** (2), 229–250.

BECH, K. H. & ANDERSSON, H. I. 1994 Very-large-scale structures in DNS. In *Direct and Large-Eddy Simulation I* (ed. P. R. Voke *et al.*), pp. 13–24. Springer.

BUTLER, K. M. & FARRELL, B. F. 1992 Three-dimensional optimal perturbations in viscous shear flow. *Phys. Fluids* **4** (8), 1637–1650.

ELLINGSEN, T. & PALM, E. 1975 Stability of linear flow. *Phys. Fluids* **18** (4), 487–488.

FARRELL, B. F. & IOANNOU, P. J. 1993 Stochastic forcing of the linearized Navier–Stokes equations. *Phys. Fluids* **5** (11), 2600–2609.

GAYME, D. F., MCKEON, B. J., BAMIEH, B., PAPACHRISTODOULOU, A. & DOYLE, J. C. 2011 Amplification and nonlinear mechanisms in plane Couette flow. *Phys. Fluids* **23** (6), 065108.

GAYME, D. F., MCKEON, B. J., PAPACHRISTODOULOU, A., BAMIEH, B. & DOYLE, J. C. 2010 A streamwise constant model of turbulence in plane Couette flow. *J. Fluid Mech.* **665**, 99–119.

GUALA, M., HOMMEMA, S. E. & ADRIAN, R. J. 2006 Large-scale and very-large-scale motions in turbulent pipe flow. *J. Fluid Mech.* **554**, 521–542.

GUSTAVSSON, L. H. 1991 Energy growth of three-dimensional disturbances in plane Poiseuille flow. *J. Fluid Mech.* **224**, 241–260.

HOYAS, S. & JIMÉNEZ, J. 2006 Scaling of the velocity fluctuations in turbulent channels up to $Re_\tau = 2003$. *Phys. Fluids* **18** (1), 011702.

HOYAS, S. & JIMÉNEZ, J. 2008 Reynolds number effects on the Reynolds-stress budgets in turbulent channels. *Phys. Fluids* **20** (10), 101511.

HUTCHINS, N. & MARUSIC, I. 2007 Evidence of very long meandering features in the logarithmic region of turbulent boundary layers. *J. Fluid Mech.* **579**, 1–28.

HWANG, Y. & COSSU, C. 2010*a* Amplification of coherent streaks in the turbulent Couette flow: an input–output analysis at low Reynolds number. *J. Fluid Mech.* **643**, 333–348.

HWANG, Y. & COSSU, C. 2010*b* Linear non-normal energy amplification of harmonic and stochastic forcing in the turbulent channel flow. *J. Fluid Mech.* **664**, 51–73.

ILLINGWORTH, S. J., MONTY, J. P. & MARUSIC, I. 2018 Estimating large-scale structures in wall turbulence using linear models. *J. Fluid Mech.* **842**, 146–162.

JOVANOVIC, M. R. & BAMIEH, B. 2005 Componentwise energy amplification in channel flows. *J. Fluid Mech.* **534**, 145–183.

KIM, J. & LIM, J. 2000 A linear process in wall-bounded turbulent shear flows. *Phys. Fluids* **12** (8), 1885–1888.

KIM, K. C. & ADRIAN, R. J. 1999 Very large-scale motion in the outer layer. *Phys. Fluids* **11** (2), 417–422.

KITOH, O., NAKABYASHI, K. & NISHIMURA, F. 2005 Experimental study on mean velocity and turbulence characteristics of plane Couette flow: low-Reynolds-number effects and large longitudinal vortical structure. *J. Fluid Mech.* **539**, 199–227.

KITOH, O. & UMEKI, M. 2008 Experimental study on large-scale streak structure in the core region of turbulent plane Couette flow. *Phys. Fluids* **20** (2), 025107.

KOMMINAHO, J., LUNDBLADH, A. & JOHANSSON, A. V. 1996 Very large structures in plane turbulent Couette flow. *J. Fluid Mech.* **320**, 259–285.

LANDAHL, M. T. 1967 A wave-guide model for turbulent shear flow. *J. Fluid Mech.* **29** (3), 441–459.

LANDAHL, M. T. 1980 A note on an algebraic instability of inviscid parallel shear flows. *J. Fluid Mech.* **98** (2), 243–251.

LEE, M. & MOSER, R. D. 2018 Extreme-scale motions in turbulent plane Couette flows. *J. Fluid Mech.* **842**, 128–145.

LEE, M. J. & KIM, J. 1991 The structure of turbulence in a simulated plane Couette flow. In *8th Symposium on Turbulent Shear Flows,* vol. 1, pp. 5.3.1–5.3.6.

MADHUSUDANAN, A., ILLINGWORTH, S. J. & MARUSIC, I. 2019 Coherent large-scale structures from the linearized Navier–Stokes equations. *J. Fluid Mech.* **873**, 89–109.

MASLOWE, S. A. 1986 Critical layers in shear flows. *Annu. Rev. Fluid Mech.* **18** (1), 405–432.

MCKEON, B. J. & SHARMA, A. S. 2010 A critical-layer framework for turbulent pipe flow. *J. Fluid Mech.* **658**, 336–382.

MONTY, J. P., HUTCHINS, N., NG, H. C. H., MARUSIC, I. & CHONG, M. S. 2009 A comparison of turbulent pipe, channel and boundary layer flows. *J. Fluid Mech.* **632**, 431–442.

MONTY, J. P., STEWART, J. A., WILLIAMS, R. C. & CHONG, M. S. 2007 Large-scale features in turbulent pipe and channel flows. *J. Fluid Mech.* **589**, 147–156.

PAPAVASSILIOU, D. V. & HANRATTY, T. J. 1997 Interpretation of large-scale structures observed in a turbulent plane Couette flow. *Intl J. Heat Fluid Flow* **18** (1), 55–69.

PIROZZOLI, S., BERNARDINI, M. & ORLANDI, P. 2014 Turbulence statistics in Couette flow at high Reynolds number. *J. Fluid Mech.* **758**, 327–343.

PIROZZOLI, S., BERNARDINI, M., VERZICCO, R. & ORLANDI, P. 2017 Mixed convection in turbulent channels with unstable stratification. *J. Fluid Mech.* **821**, 482–516.

PUJALS, G., GARCÍA-VILLALBA, M., COSSU, C. & DEPARDON, S. 2009 A note on optimal transient growth in turbulent channel flows. *Phys. Fluids* **21** (1), 015109.

REYNOLDS, W. C. & HUSSAIN, A. K. M. F. 1972 The mechanics of an organized wave in turbulent shear flow. Part 3. Theoretical models and comparisons with experiments. *J. Fluid Mech.* **54** (02), 263–288.

SCHMID, P. J. & HENNINGSON, D. S. 2001 *Stability and Transition in Shear Flows*. Springer.

SHARMA, A. S. & MCKEON, B. J. 2013 On coherent structure in wall turbulence. *J. Fluid Mech.* **728**, 196–238.

TILLMARK, N. & ALFREDSSON, P. H. 1994 Structures in turbulent plane Couette flow obtained from correlation measurements. In *Advances in Turbulence V* (ed. R. Benzi), pp. 502–507. Springer.

TILLMARK, N. & ALFREDSSON, P. H. 1998 Large scale structures in turbulent plane Couette flow. In *Advances in Turbulence VII*, pp. 59–62. Springer.

TOWNSEND, A. A. 1956 *The Structure of Turbulent Shear Flow*. Cambridge University Press.

TREFETHEN, L. N. 2008 Is Gauss quadrature better than Clenshaw–Curtis? *SIAM Rev.* **50** (1), 67–87.

TREFETHEN, L. N., TREFETHEN, A. E., REDDY, S. C. & DRISCOLL, T. A. 1993 Hydrodynamic stability without eigenvalues. *Science* **261** (5121), 578–584.

TSUKAHARA, T., KAWAMURA, H. & SHINGAI, K. 2006 DNS of turbulent Couette flow with emphasis on the large-scale structure in the core region. *J. Turbul.* **7** (19), N19.

VADAREVU, S. B., SYMON, S., ILLINGWORTH, S. J. & MARUSIC, I. 2019 Coherent structures in the linearized impulse response of turbulent channel flow. *J. Fluid Mech.* **863**, 1190–1203.

ZAKI, T. A. & DURBIN, P. A. 2005 Mode interaction and the bypass route to transition. *J. Fluid Mech.* **531**, 85–111.

ZAKI, T. A. & DURBIN, P. A. 2006 Continuous mode transition and the effects of pressure gradient. *J. Fluid Mech.* **563**, 357–388.